Simple deformation measures for Discrete elastic rods and ribbons

K Korner, Basile Audoly, K Bhattacharya

PROCEEDINGS A

rspa.royalsocietypublishing.org

Research

Article submitted to journal

Subject Areas:
mechanical engineering, mechanics

Keywords:
thin elastic rods, simulations, discrete geometry, ribbons

Author for correspondence:
Basile Audoly
e-mail:
basile.audoly@polytechnique.edu

THE ROYAL SOCIETY
PUBLISHING

Simple deformation measures for Discrete elastic rods and ribbons

K. Korner[1], B. Audoly[2] and
K. Bhattacharya[1]

[1]Division of Engineering and Applied Science, California Institute of Technology, Pasadena (CA), USA
[2]Laboratoire de Mécanique des Solides, CNRS, Institut Polytechnique de Paris, Palaiseau, France

The discrete elastic rod method (Bergou *et al.*, 2008) is a numerical method for simulating slender elastic bodies. It works by representing the centerline as a polygonal chain, attaching two perpendicular directors to each segment and defining discrete stretching, bending and twisting deformation measures and a discrete strain energy. Here, we investigate an alternative formulation of this model based on a simpler definition of the discrete deformation measures. Both formulations are equally consistent with the continuous rod model. Simple formulas for the first and second gradients of the discrete deformation measures are derived, making it easy to calculate the Hessian of the discrete strain energy. A few numerical illustrations are given. The approach is also extended to inextensible ribbons described by the Wunderlich model, and both the developability constraint and the dependence of the energy on the strain gradients are handled naturally.

1. Introduction

The geometric non-linearity of thin elastic rods gives rise to a rich range of phenomena even when the strains are small, see e.g. [1,2] for recent examples. So, the non-linear theory of rods has traditionally combined geometrical non-linearity with linear constitutive laws [3, 4]. However, recent interest has expanded beyond the linearly elastic regime, including viscous threads [5,6], plastic and visco-plastic bars [7–9], visco-elastic rods [10] and capillary elastic beams made of very soft materials [11]. Thin elastic ribbons may also be viewed in this class with a non-linear constitutive law that captures the complex deformation of the cross-sections [12–17].

The study of instabilities, especially in the presence of complex constitutive relations, requires an accurate but efficient numerical method. Here, we build on the work of Bergou *et al.* [18] to propose a numerical method that is applicable to slender elastic structures in general. To keep the presentation focused, we limit our study to *elastic* rods: both linear elastic and non-linear elastic constitutive laws are covered. Our main contribution consists in providing a discrete geometric description of slender rods. This kinematic building block is independent of the elastic constitutive law in our formulation, making the extension to inelastic constitutive laws relatively straightforward, as discussed in Section 4.

We follow the classical kinematic approach, and use the arc-length s in the undeformed configuration as a Lagrangian coordinate. We denote the centerline of the rod in the current configuration as $\boldsymbol{x}(s)$ (boldface symbols denote vectors). We introduce an orthonormal set of vectors $(\boldsymbol{d}_I(s))_{1\leqslant I\leqslant 3}$, called the *directors*, to describe the orientation of the cross-section. We impose the *adaptation condition* that the director $\boldsymbol{d}_3$ matches the unit tangent $\boldsymbol{t}$ to the centerline,

$$\boldsymbol{d}_3(s) = \boldsymbol{t}(s), \text{ where } \boldsymbol{t}(s) = \frac{\boldsymbol{x}'(s)}{|\boldsymbol{x}'(s)|}. \tag{1.1}$$

Here $\boldsymbol{x}'(s) = \partial\boldsymbol{x}/\partial s$ denotes the derivative of $\boldsymbol{x}$ with respect to the arc-length s. Note that the adaptation condition does *not* impose any restriction on the actual deformation of the rod at the microscopic scale; specifically, it does not require the deformed cross-section to be spanned by $\boldsymbol{d}_1$ and $\boldsymbol{d}_2$. Instead, it expresses the fact that the only role of the directors is to track the twisting motion of the cross-sections about the tangent. Equation (1.1) does not impose inextensibility either.

The rotation gradient $\boldsymbol{\kappa}(s)$, also known as the Darboux vector, is defined by

$$\boldsymbol{d}_I'(s) = \boldsymbol{\kappa}(s) \times \boldsymbol{d}_I(s), \qquad I = 1, 2, 3. \tag{1.2}$$

It exists and is unique since the directors are orthonormal. The deformation measures are

$$\kappa_{(I)}(s) = \boldsymbol{\kappa}(s) \cdot \boldsymbol{d}_I(s) \tag{1.3}$$

A fourth deformation measure is introduced to characterize how the centerline stretches, such as $\varepsilon(s) = \frac{1}{2}\left(\boldsymbol{x}'^2(s) - 1\right)$ (Green-Lagrange strain).

This kinematic description is common to all variants of the rod model. It is complemented by constitutive equations specifying either the stored energy density (in the case of a hyperelastic theory) or the reaction forces and moments as functions of the four deformation measures or their histories. The formulation is completed by imposing either equilibrium or balance of momenta. The resulting equations for linear elastic constitutive relations are known as the Kirchhoff equations for rods, and they can be derived variationally, see [4,19]; we will not discuss them further.

Various strategies have been proposed to simulate the equations for thin rods numerically. In approaches based on the finite-element methods, it is challenging to represent the kinematic constraint of adaptation (1.1) between the unknown centerline $\boldsymbol{x}(s)$ and the unknown rotation representing the orthonormal directors $\boldsymbol{d}_I(s)$. Another approach is based on super-helices or super-clothoids: in these high-order approaches, the bending and twisting strain measures $\kappa_{(I)}(s)$ are discretized into constant or piecewise linear functions. The result is a highly accurate method which has been successfully applied to several challenging problems [20–22]. The price to pay is that the reconstruction of the centerline in terms of the degrees of freedom is non-trivial and non-local. Additionally, some common boundary conditions, such as clamped–clamped conditions, must be treated using non-linear constraints.

A different approach, called the Discrete elastic rod method, was introduced by Bergou *et al.* [18]; see [23] for a recent primer. The discrete elastic rod method is a low-order method, which starts out by discretizing the centerline into a polygonal chain with nodes $(\boldsymbol{x}_0, \ldots, \boldsymbol{x}_N)$. The tangents and material frames $\boldsymbol{d}_I^i$ are defined on the segments, see Figure 1.1. The adaptation condition (1.1) is used to parametrize the material frames $(\boldsymbol{d}_I^i)_{1\leqslant i\leqslant 3}$ in terms of the positions

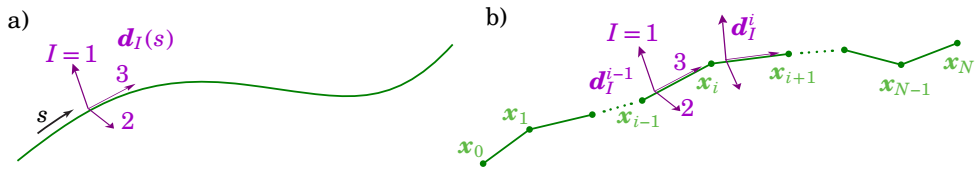

Figure 1.1. (a) A continuous elastic rod and (b) a discrete elastic rod. The adaptation condition from equations (1.1) and (2.6) is satisfied in both cases.

$(\boldsymbol{x}_{i-1}, \boldsymbol{x}_i)$ of the adjacent nodes and of a single twisting angle φ^i, as described in Section 2(d). A discrete rotation gradient is obtained by comparing the orthonormal directors from adjacent segments: this yields a differential rotation at a *vertex* between the segments, which must be projected onto a material frame to yield the bending and twisting strain measures according to equation (1.3). The material frame, however, lives on *segments*. The original Discrete elastic rod formulation worked around this difficulty by introducing an additional director frame living on the nodes, obtained by averaging the director frames from the adjacent segments [18,23]. In the present work, a different definition of the discrete bending and twisting strain measures is used, see Equations (2.11) and (2.13). This small change simplifies the formulation of the model considerably. We note that a similar measure was introduced independently in a recent work on shearable rod models [24].

Overall, the proposed formulation offers the following advantages.

- As in the original Discrete rod model, the proposed formulation eliminates two out of the three degrees of freedom associated with the directors at each node using the adaptation condition (1.1); this leads to a constraint-free formulation that uses degrees of freedom sparingly.
- The formulation of the model is concise: in particular the gradient and Hessian of the discrete elastic energy are given by the simple, closed form formulas listed in Section 3.
- The proposed deformation measures have a clear geometric interpretation: in the context of inextensible ribbons, for example, a discrete developability condition can easily be formulated in terms of the new set of discrete strains, see Section 2(b).
- The kinematic description can easily be combined with various constitutive models to produce discrete models for elastic rods, inextensible ribbons, viscous or visco-elastic rods, etc., as discussed in Section 4.

2. Discrete bending and twisting deformation measures

(a) A compendium on quaternions

Rod models make use of rotations in the three-dimensional space. These rotations are conveniently represented using quaternions. Here, we provide a brief summary of quaternions and their main properties. A complete and elementary introduction to quaternions can be found in [25].

A quaternion $q \in \mathbb{Q}$ can be seen as a pair made up of a scalar $s \in \mathbb{R}$ and a vector $\boldsymbol{v} \in \mathbb{R}^3$, $q = (s, \boldsymbol{v})$. Identifying the scalar s and the vector $\boldsymbol{v}$ with the quaternions $(s, \boldsymbol{0})$ and $(0, \boldsymbol{v})$ respectively, one has the quaternion decomposition

$$q = s + \boldsymbol{v}.$$

The product of two quaternions $q_1 = (s_1, \boldsymbol{v}_1)$ and $q_2 = (s_2, \boldsymbol{v}_2)$ is defined as

$$q_1\, q_2 = (s_1\, s_2 - \boldsymbol{v}_1 \cdot \boldsymbol{v}_2) + (s_1 \boldsymbol{v}_2 + s_2 \boldsymbol{v}_1 + \boldsymbol{v}_1 \times \boldsymbol{v}_2). \tag{2.1}$$

The product is non-commutative.

A unit quaternion $r = s + \boldsymbol{v}$ is a quaternion such that $s^2 + |\boldsymbol{v}|^2 = 1$. Unit quaternions represent rotations in the three-dimensional Euclidean space, in the following sense. Define $\bar{r} = s - \boldsymbol{v}$ as the quaternion conjugate to r. Define the action of the unit quaternion r on an arbitrary vector $\boldsymbol{w}$ as

$$r * \boldsymbol{w} = r\, \boldsymbol{w}\, \bar{r},$$

where the left-hand side defines a linear map on the set of vectors $\boldsymbol{w}$ and the right-hand side is a double product of quaternions. It can be shown that (*i*) the quaternion $r * \boldsymbol{w}$ is a pure vector, (*ii*) the mapping $\boldsymbol{w} \to r * \boldsymbol{w}$ is a rotation in Euclidean space and (*iii*) the quaternion r can be written as $r = \pm r_{\boldsymbol{n}}(\theta)$, where

$$r_{\boldsymbol{n}}(\theta) = \cos\frac{\theta}{2} + \boldsymbol{n}\, \sin\frac{\theta}{2} = \exp\frac{\boldsymbol{n}\,\theta}{2}, \tag{2.2}$$

θ is the angle of the rotation and $\boldsymbol{n}$ is a unit vector subtending the axis of rotation. Note that both unit quaternions $+r_{\boldsymbol{n}}(\theta)$ and $-r_{\boldsymbol{n}}(\theta)$ represent the same rotation.

Given two unit quaternions r_1 and r_2, consider the product $r_2\, r_1$: for any vector $\boldsymbol{w}$, the equality $(r_2\, r_1) * \boldsymbol{w} = r_2\, r_1\, \boldsymbol{w}\, \overline{r_2\, r_1} = r_2\, r_1\, \boldsymbol{w}\, \overline{r_1}\, \overline{r_2} = r_2 * (r_1 * \boldsymbol{w})$ shows that the unit quaternion $r_2\, r_1$ represents the *composition* of the rotations associated with r_1 applied first and r_2 applied last. The multiplication of unit quaternions is therefore equivalent to the composition of rotations. In view of this, we will *identify* rotations with unit quaternions. The inverse of the rotation r will accordingly be identified with the conjugate $\bar{r}$.

(b) Parallel transport

Parallel transport plays a key role in the discrete elastic rod model, by allowing one to define twistless configurations of the material frame in an intrinsic way. For two unit vectors $\boldsymbol{a}$ and $\boldsymbol{b}$ such that $\boldsymbol{b} \neq -\boldsymbol{a}$, the parallel transport from $\boldsymbol{a}$ to $\boldsymbol{b}$ is the rotation mapping $\boldsymbol{a}$ to $\boldsymbol{b}$, whose axis is along the binormal $\boldsymbol{a} \times \boldsymbol{b}$. Parallel transport can be interpreted geometrically as the rotation mapping $\boldsymbol{a}$ to $\boldsymbol{b}$ and tracing out the shortest path on the unit sphere [18].

An explicit expression of the parallel transport from $\boldsymbol{a}$ to $\boldsymbol{b}$ in terms of unit quaternions is [26]

$$p_{\boldsymbol{a}}^{\boldsymbol{b}} = \sqrt{\frac{1 + \boldsymbol{a}\cdot\boldsymbol{b}}{2}} + \frac{1}{2}\, \frac{\boldsymbol{a}\times\boldsymbol{b}}{\sqrt{\frac{1+\boldsymbol{a}\cdot\boldsymbol{b}}{2}}}. \tag{2.3}$$

The proof is as follows. First it can be verified that $p_{\boldsymbol{a}}^{\boldsymbol{b}}$ is a unit quaternion, as can be shown by using the identity $\frac{|\boldsymbol{a}\times\boldsymbol{b}|^2}{1+\boldsymbol{a}\cdot\boldsymbol{b}} = \frac{1-(\boldsymbol{a}\cdot\boldsymbol{b})^2}{1+\boldsymbol{a}\cdot\boldsymbol{b}} = 1 - \boldsymbol{a}\cdot\boldsymbol{b}$. Second, the rotation $p_{\boldsymbol{a}}^{\boldsymbol{b}}$ indeed maps $\boldsymbol{a}$ to

$$p_{\boldsymbol{a}}^{\boldsymbol{b}} * \boldsymbol{a} = p_{\boldsymbol{a}}^{\boldsymbol{b}}\, \boldsymbol{a}\, \overline{p_{\boldsymbol{a}}^{\boldsymbol{b}}} = \boldsymbol{b}, \tag{2.4}$$

as can be checked by explicit calculation. Finally, the axis of $p_{\boldsymbol{a}}^{\boldsymbol{b}}$ is indeed about the binormal $\boldsymbol{a} \times \boldsymbol{b}$: equation (2.2) shows that the vector part of the unit quaternion is aligned with the rotation axis and equation (2.3) shows that the vector part of $p_{\boldsymbol{a}}^{\boldsymbol{b}}$ is aligned with $\boldsymbol{a} \times \boldsymbol{b}$.

When the units vectors are such that $\boldsymbol{a} = -\boldsymbol{b}$, the parallel transport $p_{\boldsymbol{a}}^{\boldsymbol{b}}$ is ill-defined.

(c) Reference and current configurations

A configuration of the discrete rod is defined by a set of nodes $\boldsymbol{x}_i$ indexed by an integer i, $0 \leqslant i \leqslant N$. We consider an open rod having unconstrained endpoints $\boldsymbol{x}_0$ and $\boldsymbol{x}_N$ for the moment; alternative boundary conditions such as periodic or clamped boundary conditions are discussed later. For simplicity, we limit our attention to the case where the nodes are equally spaced in the undeformed configuration, *i.e.*, the undeformed length ℓ^j is independent of the segment index j: it is denoted as

$$\ell^j = \ell.$$

In addition to the undeformed configuration, the simulation deals with the two configurations shown in Figure 2.1.

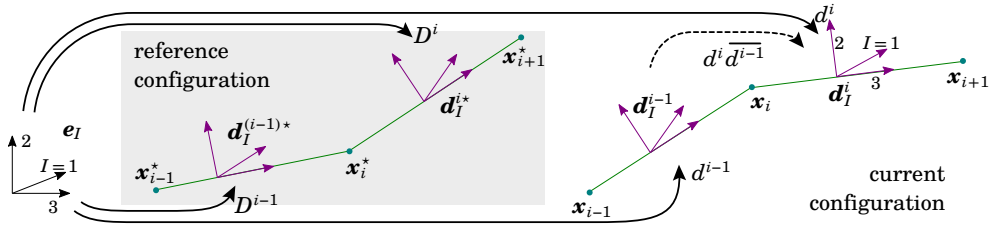

Figure 2.1. A node $\boldsymbol{x}_i$, its adjacent segments and the adjacent nodes $\boldsymbol{x}_{i\pm1}$ in reference (gray background) and current (white background) configurations. Director frames, shown in purple, are represented by a unit quaternion, whose action on the Cartesian frame $\boldsymbol{e}_I$ yields the director frame.

- **Reference configuration** (shown with a gray background in the figure). The only role of the reference configuration is to allow a parametrization of the current configuration. It does not bear any physical meaning and its choice does not affect the results of the simulations. It is chosen for convenience.
  In the reference configuration, the position of node i is denoted by $\boldsymbol{x}^\star_i$. The orthonormal frame of directors on segment i connecting nodes $\boldsymbol{x}^\star_i$ and $\boldsymbol{x}^\star_{i+1}$ is denoted as $(\boldsymbol{d}^{i\star}_I)_{I\in\{1,2,3\}}$. The adaptation condition from equation (1.1) requires that the third director $\boldsymbol{d}^{j\star}_3$ coincides with the unit tangent $\boldsymbol{T}^j$ to the segment in the reference configuration,

$$\boldsymbol{d}^{j\star}_3 = \boldsymbol{T}^j, \text{ where } \boldsymbol{T}^j = \frac{\boldsymbol{x}^\star_{j+1} - \boldsymbol{x}^\star_j}{|\boldsymbol{x}^\star_{j+1} - \boldsymbol{x}^\star_j|}. \tag{2.5}$$

- **Current configuration** (shown with a white background). The current configuration is the physical configuration of the rod and is the unknown in a simulation. It is parametrized by the degrees of freedoms (see Section 2(g)).
  In the current configuration, the centerline of the rod is defined by the node positions $\boldsymbol{x}_i$. On segment i connecting the nodes $\boldsymbol{x}_i$ and $\boldsymbol{x}_{i+1}$, the directors are denoted as $(\boldsymbol{d}^i_I)_{I\in\{1,2,3\}}$. The adaptation condition from equation (1.1) requires

$$\boldsymbol{d}^j_3 = \boldsymbol{t}^j, \text{ where } \boldsymbol{t}^j = \frac{\boldsymbol{x}_{j+1} - \boldsymbol{x}_j}{|\boldsymbol{x}_{j+1} - \boldsymbol{x}_j|}. \tag{2.6}$$

As shown in the figure, the orthonormal director frames $(\boldsymbol{d}^{j\star}_I)_{1\leqslant I\leqslant 3}$ and $(\boldsymbol{d}^j_I)_{1\leqslant I\leqslant 3}$ are represented by unit quaternions D^j and d^j, respectively, that yield the directors when applied to the Cartesian basis $\boldsymbol{e}_I$,

$$D^j * \boldsymbol{e}_I = \boldsymbol{d}^{j\star}_I, \qquad d^j * \boldsymbol{e}_I = \boldsymbol{d}^j_I \qquad \text{for } I = 1, 2, 3. \tag{2.7}$$

The quaternions $d^{j\star}$ and d^j therefore represent the rotations $\sum_{I=1}^3 \boldsymbol{d}^{j\star}_I \otimes \boldsymbol{e}_I$ and $\sum_{I=1}^3 \boldsymbol{d}^j_I \otimes \boldsymbol{e}_I$, respectively. They fully describe their respective frames.

The reference and current configurations are not assumed to be close to one another. However, our parametrization introduces a weak restriction: the reference configuration must be chosen such that the angle of the rotation $\left(d^j\,\overline{D^j}\right)$ mapping $\boldsymbol{d}^{j\star}_I$ to $\boldsymbol{d}^j_I$ does not come close to π, in any of the segments j. This condition is fulfilled by resetting periodically the reference configuration to the current configuration:

- in dynamic simulations, this reset is typically done at the end of any time step;
- in equilibrium problems, it is typically done whenever an equilibrium has been found and the load is incremented.

In principle, it is even possible to reset the reference configuration in the middle of the Newton-Raphson iteration used to update a time step (in the dynamic case) or the non-linear equilibrium (in the static case), but special care is required as this amounts to changing the parametrization of the unknown during iteration.

All the applications shown at the end of this paper deal with the static case, *i.e.*, they involve the calculation of equilibria for a series of load values: our simulations are initialized with the reference configuration $\boldsymbol{x}_i^\star$, $\boldsymbol{d}_I^{j\star}$, representing a simple starting point which is typically a straight or circular equilibrium configuration without any load (see the example description for further details). The reference configuration is reset each time an equilibrium is found.

(d) Centerline-twist representation

In this section, we introduce a parametrization that provides a concise representation of the current configuration that is at the heart of the Discrete elastic rod method. All quantities from the reference configuration, such as the node positions $\boldsymbol{x}_i^\star$, unit tangents $\boldsymbol{T}^j$, material frames $\boldsymbol{d}_3^{j\star}$ and associated rotations D^j, are known. We proceed to analyze the current configuration. A key observation is that equation (2.6) yields the tangent director $\boldsymbol{d}_3^j$ as a function of the node positions $\boldsymbol{x}_i$: if the nodes are prescribed, the full frame of directors $\boldsymbol{d}_I^j$ can only twist about this tangent. The three directors $(\boldsymbol{d}_I^j)_{1\leqslant I\leqslant 3}$ on segment j, as well as the associated unit quaternion d^j by equation (2.7), can therefore be parametrized in terms of

- the adjacent node positions $\boldsymbol{x}_j$ and $\boldsymbol{x}_{j+1}$,
- a scalar twist angle φ^j.

The parametrization used by the Discrete elastic rod method may be written as [18,27,28]

$$d^j(\boldsymbol{x}_j, \varphi^j, \boldsymbol{x}_{j+1}) = p^j(\boldsymbol{x}_j, \boldsymbol{x}_{j+1})\, r_{\boldsymbol{T}^j}(\varphi^j)\, D^j, \tag{2.8}$$

where $\boldsymbol{x}_j$ and $\boldsymbol{x}_{j+1}$ are the positions of the adjacent nodes, φ^j is the twisting angle,

$$p^j(\boldsymbol{x}_j, \boldsymbol{x}_{j+1}) = p_{\boldsymbol{T}^i}^{\boldsymbol{t}^i(\boldsymbol{x}_j, \boldsymbol{x}_{j+1})} \tag{2.9}$$

is the parallel transport from the reference unit tangent $\boldsymbol{T}^i$ to the current unit tangent $\boldsymbol{t}^i(\boldsymbol{x}_j, \boldsymbol{x}_{j+1})$ given as a function of the node positions by equation (2.6), $r_{\boldsymbol{T}^j}(\varphi^j) = \cos\frac{\varphi^j}{2} + \boldsymbol{T}^j \sin\frac{\varphi^j}{2}$ is the rotation about $\boldsymbol{T}^j$ with angle φ^j (see equation (2.2)) and D^j is the unit quaternion associated with the reference configuration of the directors (see equation (2.7)).

Using equations (2.7), (2.5) and (2.4), we have $\boldsymbol{d}_3^j = d^j(\boldsymbol{x}_j, \varphi^j, \boldsymbol{x}_{j+1}) * \boldsymbol{e}_3 = p^j(\boldsymbol{x}_j, \boldsymbol{x}_{j+1}) * (r_{\boldsymbol{T}}(\varphi^j, \boldsymbol{T}^j) * (D^j * \boldsymbol{e}_3)) = p_{\boldsymbol{T}^i}^{\boldsymbol{t}^i} * (r_{\boldsymbol{T}^j}(\varphi^j) * \boldsymbol{T}^j) = p_{\boldsymbol{T}^i}^{\boldsymbol{t}^i} * \boldsymbol{T}^j = \boldsymbol{t}^j$: the parametrization (2.8) of the directors satisfies the adaptation constraint in (2.6) automatically.

This yields a parametrization of the rod in terms of the degrees of freedom vector

$$\boldsymbol{X} = (\boldsymbol{x}_0, \varphi^0, \boldsymbol{x}_1, \varphi^1, \boldsymbol{x}^2, \cdots, \boldsymbol{x}_{n-1}, \varphi^{n-1}, \boldsymbol{x}_n), \tag{2.10}$$

where the node positions $\boldsymbol{x}_i$ are read off directly from $\boldsymbol{X}$ and the directors are reconstructed using equations (2.7) and (2.8). This is called the *centerline-twist representation*.

As observed in Section 2(b), the parallel transport in equation (2.9) is singular if $\boldsymbol{t}^i(\boldsymbol{x}_j, \boldsymbol{x}_{j+1}) = -\boldsymbol{T}^i$, *i.e.*, if any one of the tangents flips by an angle π between the reference and current configuration. The periodic reset of the reference configuration described earlier in Section 2(c) prevents this from happening.

Note that, in the original paper of [18], parallel transport was used to move the directors from one segment to an adjacent segment (*spatial* parallel transport). This makes the directors dependent on the degrees of freedom associated with all the nodes and segments located on one side of the directors. Here, as in subsequent work by the same authors [27,28], we use parallel transport 'in time': in equation (2.8), $p^j(\boldsymbol{x}_j, \boldsymbol{x}_{j+1})$ serves to parametrize the directors in the current configuration in terms of the same set of directors in the reference configuration. With this

approach, the directors are a function of the *local* degrees of freedom, as implied by the notation $d^j(\boldsymbol{x}_j, \varphi^j, \boldsymbol{x}_{j+1})$ in equation (2.8).

(e) Lagrangian rotation gradient

The rotation mapping one director frame $(\boldsymbol{d}_I^{i-1})_{I=1,2,3}$ to the adjacent director frame $(\boldsymbol{d}_I^i)_{I=1,2,3}$ is shown by the dashed arrow on top of Figure 2.1. It captures the variation of the frame along the rod, and it is the discrete counterpart of the rotation gradient $\boldsymbol{\kappa}(s)$ introduced in equation (1.2). Using equation (2.7), it can be written as the composition of the rotations $\overline{d^{i-1}}$ and d^i:

$$d^i\,\overline{d^{i-1}} : \boldsymbol{d}_I^{i-1} \mapsto \boldsymbol{d}_I^i.$$

This rotation is an Eulerian quantity: like its continuous counterpart $\boldsymbol{\kappa}(S)$, it is not invariant when the rod rotates rigidly. The following, however, is a Lagrangian version q_i of the rotation gradient that is invariant by rigid-body rotations,

$$q_i(\boldsymbol{x}_{i-1}, \varphi^{i-1}, \boldsymbol{x}_i, \varphi^i, \boldsymbol{x}_{i+1}) := \overline{d^{i-1}}(\boldsymbol{x}_{i-1}, \varphi^{i-1}, \boldsymbol{x}_i)\, d^i(\boldsymbol{x}_i, \varphi^i, \boldsymbol{x}_{i+1}). \tag{2.11}$$

Here, we depart from earlier work on discrete elastic rods [18], which used $q_i := q_i^{\text{avg}} = \bar{d}_i^\dagger\,(d^i\,\overline{d^{i-1}})\,d_i^\dagger$ instead, where $d_i^\dagger$ is some average of the adjacent frames d^{i-1} and d^i. A definition of the rotation gradient similar to (2.11) has been used in the context of shearable rods [24] and in a purely geometric analysis of discrete rods [26].

We now explain why this definition represents a Lagrangian rotation gradient. One way to define a Lagrangian rotation gradient is to pull back the Eulerian rotation gradient $d^i\,\overline{d^{i-1}}$ to the reference configuration. However, the discreteness of our representation raises a difficulty: the frames are defined on the segment while the Eulerian rotation gradient $d^i\,\overline{d^{i-1}}$ is defined on the nodes. So, we could use the frame associated with the segment on the left of the node for the pull-back by defining $q_i^{\text{left}} = \overline{d^{i-1}}\,(d^i\,\overline{d^{i-1}})\,d^{i-1}$, but this biases the choice to the left. Or, we could use the right counter-part, $q_i^{\text{right}} = \overline{d^i}\,(d^i\,\overline{d^{i-1}})\,d^i$, but this biases the choice to the right. However, these biases are apparent only: elementary calculations show that these are in fact identical,

$$q_i^{\text{left}} = \overline{d^{i-1}}\,d^i\,\left(\overline{d^{i-1}}\,d^{i-1}\right) = \overline{d^{i-1}}\,d^i = q_i, \quad q_i^{\text{right}} = \left(\overline{d^i}\,d^i\right)\,\overline{d^{i-1}}\,d^i = \overline{d^{i-1}}\,d^i = q_i, \tag{2.12}$$

thereby justifying our definition.

The unit quaternion q_i introduced in equation (2.11) is the discrete analogue of the pull-back $(\boldsymbol{e}_I \otimes \boldsymbol{d}_I(s)) \cdot \boldsymbol{\kappa}(s)$ of the rotation gradient $\boldsymbol{\kappa}(s)$ used in the continuous rod theory, whose components $\kappa_J(s) = \boldsymbol{e}_J \cdot [(\boldsymbol{e}_I \otimes \boldsymbol{d}_I(s)) \cdot \boldsymbol{\kappa}(s)] = \boldsymbol{d}_J(s) \cdot \boldsymbol{\kappa}(s)$ define the bending and twisting measures. In the following section, bending and twisting are similarly extracted from the unit quaternion q_i.

(f) Bending and twisting deformation measures

The discrete bending and twisting deformation measures are defined as the components of the pure vector,

$$\boldsymbol{\kappa}_i(\boldsymbol{x}_{i-1}, \varphi^{i-1}, \boldsymbol{x}_i, \varphi^i, \boldsymbol{x}_{i+1}) = q_i - \overline{q}_i. \tag{2.13}$$

This $\boldsymbol{\kappa}_i$ is twice the vector part $\mathcal{I}(q_i) = \frac{q_i - \overline{q}_i}{2}$ of the quaternion q_i, which shows that it is indeed a vector. Let $\kappa_{i,I}$ denote its components in the Cartesian basis, such that $\boldsymbol{\kappa}_i = \sum_{I=1}^3 \kappa_{i,I}\,\boldsymbol{e}_I$. The first two components, $\kappa_{i,1}$ and $\kappa_{i,2}$, can be interpreted as measures of bending about the transverse directors $\boldsymbol{d}_1^j$ and $\boldsymbol{d}_2^j$, while the third component, $\kappa_{i,3}$, is a discrete measure of twisting. Like q_i, these are *integrated* versions of their smooth counterparts that are proportional to the discretization length ℓ; this will be taken into account when setting up a discrete strain energy.

(g) Summary

The current configuration is reconstructed in terms of the degrees of freedom $\boldsymbol{X}$ from equation (2.10) as follows:

- the node positions $\boldsymbol{x}_i$ are directly extracted from $\boldsymbol{X}$, see equation (2.10),
- the unit tangents $\boldsymbol{t}^j(\boldsymbol{x}_j, \boldsymbol{x}_{j+1})$ are obtained from equation (2.6),
- parallel transport $p^j(\boldsymbol{x}_j, \boldsymbol{x}_{j+1})$ is obtained by combining equations (2.9) and (2.3),
- the director frames $d^j(\boldsymbol{x}_j, \varphi^j, \boldsymbol{x}_{j+1})$ are obtained from equation (2.8),
- the rotation gradient $q_i(\boldsymbol{x}_{i-1}, \varphi^{i-1}, \boldsymbol{x}_i, \varphi^i, \boldsymbol{x}_{i+1})$ is available from equation (2.11),
- the bending and twisting deformation vector $\boldsymbol{\kappa}_i(\boldsymbol{x}_{i-1}, \varphi^{i-1}, \boldsymbol{x}_i, \varphi^i, \boldsymbol{x}_{i+1})$ is calculated from equation (2.13).

Finally, a possible definition of the discrete stretching measure on segment j joining nodes $\boldsymbol{x}_j$ and $\boldsymbol{x}_{j+1}$ is

$$\varepsilon^j(\boldsymbol{x}_j, \boldsymbol{x}_{j+1}) = \frac{1}{2}\left(\frac{(\boldsymbol{x}_{j+1} - \boldsymbol{x}_j)^2}{\ell} - \ell\right), \tag{2.14}$$

see for instance [10]. Here, ℓ denotes the undeformed length of the segments, which is different from the length $|\boldsymbol{x}^\star_{j+1} - \boldsymbol{x}^\star_j|$ in the reference configuration. This discrete stretching measure is an integrated version of the continuous strain $\varepsilon(S)$, like the discrete bending and twisting deformation measures $\kappa_{i,I}$. The particular definition of the stretching measure ε^j in equation (2.14) requires the evaluation of the *squared* norm and not of the norm itself, which simplifies the calculation of the gradient significantly.

(h) Interpretation of the discrete deformation measures

We now show that the discrete deformation measures (up to a minor rescaling) may be interpreted as the rotation that transports the director frame from one segment to the next.

Consider the function ψ

$$\psi(t) = \frac{\arcsin(t/2)}{t/2} \quad \text{for } 0 \leqslant t \leqslant 2, \tag{2.15}$$

and note that $\psi(t) \approx 1$ for $t \ll 1$ (See supplementary information for a plot of this function). Define the *adjusted deformation measure* to be

$$\omega_{i,J} = \psi(|\boldsymbol{\kappa}_i|)\, \boldsymbol{\kappa}_i \cdot \boldsymbol{e}_J. \tag{2.16}$$

This is well defined for all values of κ since $|\boldsymbol{\kappa}_i| = |q_i - \overline{q}_i| \leqslant 2\,|q_i| = 2$. This rescaling is insignificant in the continuum limit where $d^{i-1} \approx d^i$, $q_i \approx 1$ and $|\boldsymbol{\kappa}_i| \ll 1$, implying $\psi(|\boldsymbol{\kappa}_i|) \approx 1$. Even for moderate values of $|\boldsymbol{\kappa}_i|$, the original and adjusted deformation measures are not very different, $\omega_{i,J} \approx \boldsymbol{\kappa}_i \cdot \boldsymbol{e}_J$, as the variations of the function ψ are bounded by $1 \leqslant \psi(t) \leqslant \pi/2$.

The adjusted deformation measure has a simple geometric interpretation. We start from the decomposition (2.2) of the rotation gradient $q_i = r_{\boldsymbol{n}_i}(\theta_i) = \cos\frac{\theta_i}{2} + \boldsymbol{n}_i \sin\frac{\theta_i}{2} = \exp\frac{\boldsymbol{n}_i\theta_i}{2}$, where $\boldsymbol{n}_i$ is a unit vector aligned with the axis of the rotation q_i and θ_i is the angle of this rotation, $0 \leqslant \theta \leqslant \pi$. In view of equation (2.13), $\boldsymbol{\kappa}_i = q_i - \overline{q}_i = 2\sin\frac{\theta_i}{2}\,\boldsymbol{n}_i$. In particular, $|\boldsymbol{\kappa}_i| = 2\sin\frac{\theta_i}{2}$ and so $\psi(|\boldsymbol{\kappa}_i|) = \frac{\theta_i/2}{\sin(\theta_i/2)}$ from equation (2.15). The adjusted strain is then $\omega_{i,J}\,\boldsymbol{e}_J = \psi(|\boldsymbol{\kappa}_i|)\,\boldsymbol{\kappa}_i = \frac{\theta_i/2}{\sin(\theta_i/2)}\,2\sin\frac{\theta_i}{2}\,\boldsymbol{n}_i = \theta_i\,\boldsymbol{n}_i$; in effect, the adjustment factor $\psi(|\boldsymbol{\kappa}_i|)$ transforms $\boldsymbol{\kappa}_i = 2\,\mathcal{I}(q_i)$ (twice the vector part of q_i) into $\omega_{i,J}\,\boldsymbol{e}_J = \theta_i\,\boldsymbol{n}_i = 2\,\log q_i$ (twice its logarithm).

Now, rewriting $q_i = \overline{d^{i-1}}\,d^i = \overline{d^{i-1}}\left(d^i\,\overline{d^{i-1}}\right)d^{i-1} = q_i^{\text{right}}$, one sees that q_i is conjugate to $d^i\,\overline{d^{i-1}}$. Combining with $q_i = \cos\frac{\theta_i}{2} + \boldsymbol{n}_i\sin\frac{\theta_i}{2}$, we have $d^i\,\overline{d^{i-1}} = d^{i-1}\,q_i\,\overline{d^{i-1}} = \cos\frac{\theta_i}{2} + (d^{i-1} * \boldsymbol{n}_i)\sin\frac{\theta_i}{2} = \exp\frac{(d^{i-1} * \boldsymbol{n}_i)\,\theta_i}{2}$; as is well known, the conjugate rotation $d^i\,\overline{d^{i-1}}$ has the same angle θ_i as the original rotation q_i and its axis is obtained by applying the rotation d^{i-1} to the

original axis. This can be rewritten as

$$d^i = \exp\left(\frac{\boldsymbol{\Omega}_i}{2}\right) d^{i-1} \tag{2.17}$$

where $\boldsymbol{\Omega}_i = d^{i-1} * \boldsymbol{n}_i\,\theta_i = d^{i-1} * \omega_{i,J}\,\boldsymbol{e}_J = \omega_{i,J}\,\boldsymbol{d}_J^{i-1}$ is a (finite) rotation vector. Similar relations have been derived in the work of [26]. Repeating the same argument with $q_i = \overline{d^{i-1}}\,d^i = \overline{d^i}\,(d^i\,\overline{d^{i-1}})\,d^i = q_i^{\text{left}}$, one can show that the vector $\boldsymbol{\Omega}$ has the same decomposition in the other director frame, $\boldsymbol{\Omega}_i = \omega_{i,J}\,\boldsymbol{d}_J^i$,

$$\boldsymbol{\Omega}_i = \omega_{i,J}\,\boldsymbol{d}_J^{i-1} = \omega_{i,J}\,\boldsymbol{d}_J^i. \tag{2.18}$$

Equations (2.17–2.18) show that *the adjusted deformation measures $\omega_{i,J}$ are the components of the rotation vector $\boldsymbol{\Omega}_i$ that maps one set of director frame $(\boldsymbol{d}_I^{i-1})_{I=1,2,3}$ to the other one $(\boldsymbol{d}_I^i)_{I=1,2,3}$* across the vertex $\boldsymbol{x}_i$. Remarkably, these components can be calculated in any one of the adjacent director frame as they are identical.

One could build a Discrete elastic rod model based on the adjusted deformation measure $\omega_{i,J}\,\boldsymbol{e}_J = 2\,\overline{d^{i-1}} * \log\left(d^i\,\overline{d^{i-1}}\right) = 2\,\overline{d^i} * \log\left(d^i\,\overline{d^{i-1}}\right)$ instead of the deformation measure $\boldsymbol{\kappa}_i$ proposed in Section 2(f). The benefit is that $\omega_{i,J}$ have an even simpler interpretation, see equations (2.17–2.18). The drawback is that the function ψ gets involved in the calculation of the strain, resulting in cumbersome formulas for the strain gradients (Section 3). Therefore, we continue to use the original deformation measures.

3. Variations of the discrete deformation measures

In this section, we present explicit formulae for the first and second derivatives of the deformation measures $\boldsymbol{\kappa}_i$ (summarized in Section 2(g)) with respect to $\boldsymbol{X}$. The first gradient is required for determination of the internal forces, which are the first gradient of the strain energy. The availability of the second gradient in analytical form makes it possible to use implicit time-stepping methods (in dynamic problems) or to evaluate the Hessian for second order methods (in static problems).

Our notation for variations is first introduced based on a simple example. For a function $\boldsymbol{y} = \boldsymbol{f}(\boldsymbol{x})$ taking a vector argument $\boldsymbol{x}$ and returning a vector $\boldsymbol{y}$, the first variation is the linear mapping $\delta\boldsymbol{x} \mapsto \delta\boldsymbol{y} = \boldsymbol{f}'(\boldsymbol{x}) \cdot \delta\boldsymbol{x}$, where $\delta\boldsymbol{x}$ is a perturbation to $\boldsymbol{x}$ and $\boldsymbol{f}'(\boldsymbol{x})$ is the gradient matrix. To compute the second variation, we start from $\delta\boldsymbol{y} = \boldsymbol{f}'(\boldsymbol{x}) \cdot \delta\boldsymbol{x}$, perturb the argument $\boldsymbol{x}$ of $\boldsymbol{f}'$ as $\boldsymbol{x} + \delta\boldsymbol{x}$ and linearize the result as $\boldsymbol{f}'(\boldsymbol{x} + \delta\boldsymbol{x}) \cdot \delta\boldsymbol{x} \approx \boldsymbol{f}'(\boldsymbol{x}) \cdot \delta\boldsymbol{x} + \boldsymbol{f}''(\boldsymbol{x}) : (\delta\boldsymbol{x} \otimes \delta\boldsymbol{x})$. Here, the second variation is defined as the second order term $\delta^2\boldsymbol{y} := \boldsymbol{f}''(\boldsymbol{x}) : (\delta\boldsymbol{x} \otimes \delta\boldsymbol{x})$, where $\boldsymbol{f}''(\boldsymbol{x})$ is the Hessian. By construction, $\delta^2\boldsymbol{y}$ is a quadratic form of $\delta\boldsymbol{x}$.

In this section, the reference configuration is fixed and the degrees of freedom are perturbed by $\delta\boldsymbol{X} = (\dots, \delta\boldsymbol{x}_i, \delta\varphi^i, \dots)$. We simply present the final results; the detailed calculations are cumbersome but straightforward, and are provided as supplementary material.

- **Unit tangents** $\boldsymbol{t}^i = (\boldsymbol{x}_{i+1} - \boldsymbol{x}_i)/|\boldsymbol{x}_{i+1} - \boldsymbol{x}_i|$ from equation (2.6),

$$\begin{aligned} \delta\boldsymbol{t}^i &= \frac{\boldsymbol{I} - \boldsymbol{t}^i \otimes \boldsymbol{t}^i}{|\boldsymbol{x}_{i+1} - \boldsymbol{x}_i|} \cdot (\delta\boldsymbol{x}_{i+1} - \delta\boldsymbol{x}_i) \\ \delta^2\boldsymbol{t}^i &= -\frac{\boldsymbol{\tau}^i + (\boldsymbol{\tau}^i)^{T(132)} + (\boldsymbol{\tau}^i)^{T(231)}}{|\boldsymbol{x}_{i+1} - \boldsymbol{x}_i|^2} : ((\delta\boldsymbol{x}_{i+1} - \delta\boldsymbol{x}_i) \otimes (\delta\boldsymbol{x}_{i+1} - \delta\boldsymbol{x}_i)), \end{aligned} \tag{3.1}$$

  where $\boldsymbol{I}$ is the identity matrix, $\boldsymbol{\tau}^i$ is the third-order tensor $\boldsymbol{\tau}^i = (\boldsymbol{I} - \boldsymbol{t}^i \otimes \boldsymbol{t}^i) \otimes \boldsymbol{t}^i$ and the colon denotes the double contraction of the *last* two indices of the rank 3 tensor on the left-hand side. For any permutation (n_1, n_2, n_3) of $(1, 2, 3)$, $T(n_1, n_2, n_3)$ denotes the generalized transpose of a rank 3 tensor $\boldsymbol{\mu}$ such that $\mu_{i_1 i_2 i_3}^{T(n_1 n_2 n_3)} = \mu_{i_{n_1} i_{n_2} i_{n_3}}$.

- **Parallel transport** $p^i = p^{\boldsymbol{t}^i}_{\boldsymbol{T}^i}$ from equations (2.9) and (2.3),

$$\begin{aligned} \delta\hat{\boldsymbol{p}}^i &= \left((\boldsymbol{t}^i)_\times - \tfrac{\boldsymbol{t}^i\otimes\boldsymbol{k}^i}{2}\right)\cdot\delta\boldsymbol{t}^i \\ \delta^2\hat{\boldsymbol{p}}^i &= \left((\boldsymbol{t}^i)_\times - \tfrac{\boldsymbol{t}^i\otimes\boldsymbol{k}^i}{2}\right)\cdot\delta^2\boldsymbol{t}^i + \left(\delta\boldsymbol{t}^i\cdot\tfrac{\boldsymbol{k}^i\otimes\boldsymbol{T}^i+\boldsymbol{T}^i\otimes\boldsymbol{k}^i}{4\,(1+\boldsymbol{T}^i\cdot\boldsymbol{t}^i)}\cdot\delta\boldsymbol{t}^i\right)\boldsymbol{t}^i - (\delta\boldsymbol{t}^i\otimes\delta\boldsymbol{t}^i)\cdot\tfrac{\boldsymbol{k}^i}{2}, \end{aligned} \tag{3.2}$$

  where, for any vector $\boldsymbol{a}$, $\boldsymbol{a}_\times$ is the linear operator

$$\boldsymbol{a}_\times : \boldsymbol{u} \mapsto \boldsymbol{a}\times\boldsymbol{u} \tag{3.3}$$

  and $\boldsymbol{k}^i$ is the binormal defined by

$$\boldsymbol{k}^i = \frac{2\,\boldsymbol{T}^i\times\boldsymbol{t}^i}{1+\boldsymbol{T}^i\cdot\boldsymbol{t}^i}\,. \tag{3.4}$$

- **Directors rotation** d^i from equation (2.8),

$$\begin{aligned} \delta\hat{\boldsymbol{d}}^i &= \delta\varphi^i\boldsymbol{t}^i + \delta\hat{\boldsymbol{p}}^i \\ \delta^2\hat{\boldsymbol{d}}^i &= \delta\varphi^i\,\delta\boldsymbol{t}^i + \delta^2\hat{\boldsymbol{p}}^i. \end{aligned} \tag{3.5}$$

- **Rotation gradient** q_i from equation (2.11),

$$\begin{aligned} \delta\hat{\boldsymbol{q}}_i &= \overline{d^{i-1}} * (\delta\hat{\boldsymbol{d}}^i - \delta\hat{\boldsymbol{d}}^{i-1}) \\ \delta^2\hat{\boldsymbol{q}}_i &= \overline{d^{i-1}} * (\delta^2\hat{\boldsymbol{d}}^i - \delta^2\hat{\boldsymbol{d}}^{i-1}) + \delta\hat{\boldsymbol{q}}_i\times(\overline{d^{i-1}} * \delta\hat{\boldsymbol{d}}^{i-1}). \end{aligned} \tag{3.6}$$

- **Discrete bending and twisting strain measure vector** $\boldsymbol{\kappa}_i$ from equation (2.13),

$$\begin{aligned} \delta\boldsymbol{\kappa}_i &= \mathcal{I}\,(\delta\hat{\boldsymbol{q}}_i\,q_i) \\ \delta^2\boldsymbol{\kappa}_i &= \mathcal{I}\left(\left(\delta^2\hat{\boldsymbol{q}}_i - \tfrac{\delta\hat{\boldsymbol{q}}_i\cdot\delta\hat{\boldsymbol{q}}_i}{2}\right)q_i\right), \end{aligned} \tag{3.7}$$

  where $\mathcal{I}(q) = \frac{q-\overline{q}}{2}$ denotes the vector part of a quaternion q.

- **Stretching measure** ε^i from equation (2.14),

$$\begin{aligned} \delta\varepsilon^i &= \tfrac{\boldsymbol{x}_{i+1}-\boldsymbol{x}_i}{\ell}\cdot(\delta\boldsymbol{x}_{i+1} - \delta\boldsymbol{x}_i), \\ \delta^2\varepsilon^i &= \tfrac{1}{\ell}\,(\delta\boldsymbol{x}_{i+1} - \delta\boldsymbol{x}_i)\cdot(\delta\boldsymbol{x}_{i+1} - \delta\boldsymbol{x}_i). \end{aligned} \tag{3.8}$$

In these formulae, the first and second variations of the rotations p^i, d^i and q_i are not captured by quaternions but by regular *vectors*, bearing a hat, such as $\delta\hat{\boldsymbol{p}}^i$, $\delta^2\hat{\boldsymbol{p}}^i$, $\delta\hat{\boldsymbol{d}}^i$, etc. Equations (3.1–3.8) involve standard calculations from Euclidean geometry: the more advanced quaternion calculus is only required in the proof given in the supplementary materials.

Equations (3.1–3.8) suffice to calculate the strain gradients. They can be implemented easily and efficiently using standard libraries for vector and matrix algebra. These formulas for the first and second gradient of strain are considerably simpler than those applicable to the discrete strain measures used in earlier work on Discrete elastic rods [2,10,18,28].

In equations (3.1–3.8), the perturbations to the degrees of freedom such as $\delta\boldsymbol{x}_i$ and $\delta\varphi^i$ are dummy variables. The first-order variations such as $\delta\boldsymbol{t}^i$, $\delta\hat{\boldsymbol{p}}^i$ must be represented numerically as linear forms, by storing their coefficients as vectors. Similarly, the second-order variations such as $\delta^2\boldsymbol{t}^i$, $\delta^2\hat{\boldsymbol{p}}^i$, etc. are represented as quadratic forms, whose coefficients are stored as sparse symmetric matrices; the reader is referred to [10] for further details on this aspect of implementation. All these coefficients depend on the current configuration and must be updated whenever the degrees of freedom $\boldsymbol{X}$ or the reference configuration change.

These vectors and symmetric matrices should be stored at an appropriate place in the data structure representing the Discrete elastic rod. The tensors representing $\delta\boldsymbol{t}^i$, $\delta\hat{\boldsymbol{p}}^i$, $\delta^2\hat{\boldsymbol{p}}^i$ and $\delta^2\hat{\boldsymbol{d}}^i$ depend on the perturbations $\delta\boldsymbol{x}_i$ and $\delta\boldsymbol{x}_{i+1}$ to the nodes adjacent to a given segment, and therefore are best stored in the data structure representing segments, which have access naturally to the degrees of freedom of the adjacent nodes. The quantities $\delta\hat{\boldsymbol{d}}^i$ and $\delta^2\hat{\boldsymbol{d}}^i$ make use of the twisting angle $\delta\varphi^i$ in addition to the adjacent nodes $\delta\boldsymbol{x}_i$ and $\delta\boldsymbol{x}_{i+1}$, and should be stored in the

data structure representing the material frame attached to a particular segment. The quantities $\delta\hat{\boldsymbol{q}}_i$, $\delta\boldsymbol{\kappa}_i$, $\delta^2\hat{\boldsymbol{q}}_i$ and $\delta^2\boldsymbol{\kappa}_i$ are best stored in a data structure representing an elastic hinge at a node that depends on the material frames at the adjacent segments.

4. Constitutive models

The discrete kinematics from Sections 2 and 3 can be combined with a variety of constitutive laws to produce discrete numerical models for rods that are elastic, viscous, visco-elastic, etc.: the procedure has been documented in previous work, and is similar to the general approach used in finite-element analysis. Elastic problems are treated by introducing a strain energy function $U(\boldsymbol{X})$, whose gradient with respect to $\boldsymbol{X}$ yields the negative of the discrete elastic forces [10,18]; while viscous problems are treated by introducing a discrete Rayleigh potential $U(\boldsymbol{X},\dot{\boldsymbol{X}})$,whose gradient with respect to velocities $\dot{\boldsymbol{X}}$ yields discrete viscous forces [5,27,28]. More advanced constitutive models such as visco-elastic laws can be treated by variational constitutive updates of a discrete potential that makes use of the same discrete deformation measures [10]. In [10], it is emphasized that these different constitutive models can be implemented *independently* of the geometric definition of discrete deformation measures. Using this decoupled approach, it is straightforward to combine the kinematic element proposed in the present work with the constitutive element from previous work. We illustrate this with the classical, linearly elastic rod in Section 4(a) (Kirchhoff rod model), and a discrete inextensible ribbon model in Section 4(b) (Wunderlich model). The latter is a novel application of the Discrete elastic rod method.

(a) Elastic rods (Kirchhoff model)

The classical, continuous theory of elastic rods uses a strain energy functional $U[\boldsymbol{\kappa}] = \int_0^L E(\kappa_{(1)}(s),\kappa_{(2)}(s),\kappa_{(3)}(s))\,\mathrm{d}s$, where $\kappa_{(I)}(s) = \boldsymbol{\kappa}(s)\cdot\boldsymbol{d}_I(s)$ are the components of the rotation gradient in the frame of directors, see equation (1.3). For an inextensible, linearly elastic rod made of a Hookean material with natural curvature $\kappa_{(0)}$, for instance, the strain energy density is

$$E(\kappa_{(1)}(s),\kappa_{(2)}(s),\kappa_{(3)}(s)) = \frac{1}{2}\,Y\,I_1\,\kappa_{(1)}^2 + \frac{1}{2}\,Y\,I_2\,(\kappa_{(2)}-\kappa_{(0)})^2 + \frac{1}{2}\,\mu\,J\,\kappa_{(3)}^2 \tag{4.1}$$

where Y and μ are, respectively, the Young modulus and the shear modulus of the material, I_1 and I_2 are the geometric moments of inertia of the cross-section and J is the torsional constant.

In the discrete setting, we introduce a strain energy $\sum_i E_i(\boldsymbol{\kappa}_i)$, where the sum runs over all interior nodes i. The strain energy assigned to an interior node i is defined in terms of the strain energy density as

$$E_i(\boldsymbol{\kappa}_i) = \ell\,E\left(\frac{\boldsymbol{\kappa}_i}{\ell}\right) \tag{4.2}$$

(no implicit sum over i), where ℓ is the undeformed length of the segments for a uniform mesh. The factor ℓ in the argument of E takes care of the fact that $\boldsymbol{\kappa}_i$ is an integrated quantity, *i.e.*, it is $\frac{\boldsymbol{\kappa}_i}{\ell}\cdot\boldsymbol{e}_J$ and not just $\boldsymbol{\kappa}_i\cdot\boldsymbol{e}_J$ that converges to the continuous strain $\kappa_{(J)}(s)$; for a non-uniform grid, this ℓ would need to be replaced with the Voronoi length associated with the interior vertex i in the undeformed configuration. The factor ℓ in factor of E in equation (4.2) ensures that the discrete sum $\sum_i E_i = \sum_i \ell\,E$ converges to the integral $\int_0^L E\,\mathrm{d}s = U$ [18].

Consider, for instance, an equilibrium problem with dead forces $\boldsymbol{F}_i$ on the nodes: it is governed by the total potential energy $\Phi(\boldsymbol{X})$ defined in terms of $\boldsymbol{X} = (\boldsymbol{x}_0,\varphi_0,\ldots,\varphi_{N-1},\boldsymbol{x}_N)$ as

$$\Phi(\boldsymbol{X}) = \sum_{i=1}^{N-1} E_i(\boldsymbol{\kappa}_i(\boldsymbol{x}_{i-1},\varphi^{i-1},\boldsymbol{x}_i,\varphi^i,\boldsymbol{x}_{i+1})) - \sum_{i=0}^{N}\boldsymbol{F}_i\cdot\boldsymbol{x}_i. \tag{4.3}$$

This energy is minimized subject to the inextensibility constraints

$$\forall i\in(0,N-1)\qquad \varepsilon^j(\boldsymbol{x}_j,\boldsymbol{x}_{j+1}) = 0. \tag{4.4}$$

In equations (4.3–4.4), the elastic deformation measures $\boldsymbol{\kappa}_i$ and ε^j are reconstructed in terms of the unknown $\boldsymbol{X}$ by the method described in Section 2, as expressed by the notation $\boldsymbol{\kappa}_i(\boldsymbol{x}_{i-1}, \varphi^{i-1}, \boldsymbol{x}_i, \varphi^i, \boldsymbol{x}_{i+1})$ and $\varepsilon^j(\boldsymbol{x}_j, \boldsymbol{x}_{j+1})$.

In the case of dead forces, the first and second variations of the total potential energy are derived as

$$\begin{aligned} \delta\Phi &= \sum_{i=1}^{N-2} \frac{\partial E_i}{\partial \boldsymbol{\kappa}_i} \cdot \delta\boldsymbol{\kappa}_i - \sum_{i=0}^{N-1} \boldsymbol{F}_i \cdot \delta\boldsymbol{x}_i \\ \delta^2\Phi &= \sum_{i=1}^{N-2} \left(\delta\boldsymbol{\kappa}_i \cdot \frac{\partial^2 E_i}{\partial \boldsymbol{\kappa}_i^2} \cdot \delta\boldsymbol{\kappa}_i + \frac{\partial E_i}{\partial \boldsymbol{\kappa}_i} \cdot \delta^2\boldsymbol{\kappa}_i \right), \end{aligned} \tag{4.5}$$

see for instance [10]. Here, $\frac{\partial E_i}{\partial \boldsymbol{\kappa}_i}$ and $\frac{\partial^2 E_i}{\partial \boldsymbol{\kappa}_i^2}$ are, respectively, the internal stress and tangent elastic stiffness produced by the elastic constitutive model $E_i(\boldsymbol{\kappa}_i)$. The two terms appearing in parentheses on the right-hand side of $\delta^2\Phi$ are known as the elastic and geometric stiffness, respectively. The first and second variations of the strain, $\delta\boldsymbol{\kappa}_i$ and $\delta^2\boldsymbol{\kappa}_i$, are available from Section 3: the equilibrium can be solved using numerical methods that require evaluations of the Hessian of the energy. Note that the Hessian can be represented as a sparse matrix owing to the local nature of the energy contributions $E_i(\boldsymbol{\kappa}_i(\boldsymbol{x}_{i-1}, \varphi^{i-1}, \boldsymbol{x}_i, \varphi^i, \boldsymbol{x}_{i+1}))$ in equation (4.3).

In the applications presented in the forthcoming sections, we find equilibrium configurations by minimizing $\Phi(\boldsymbol{X})$ in equation (4.3) using the sequential quadratic programming (SQP) method described by [29]; it is an extension of the Newton method for non-linear optimization problems, which can handle the non-linear constraints in equation (4.4). It requires the evaluation of the first and second gradients of the energy Φ, see equation (4.5), and of the first gradient of the constraints that are available from equation (3.8). We used an in-house implementation of the SQP method in the `C++` language, with matrix inversion done using the `SimplicialLDLT` method available from the Eigen library [30].

(b) Inextensible elastic ribbons (Wunderlich model)

Ribbons made up of material that are sensitive to light [31,32] or temperature change [33] have been used to design lightweight structures that can be actuated. They are easy to fabricate, typically by cutting out a thin sheet of material, and their thin geometry can turn the small strains produced by actuation into large-amplitude motion. For this reason, there has been a surge of interest towards mechanical models for elastic ribbons recently. When the width-to-thickness ratio of a ribbon cross-section is sufficiently large, its mid-surface is effectively inextensible. Sadowsky [12] has proposed a one-dimensional mechanical model for inextensible ribbons. Sadowsky model is one-dimensional but differs from classical rod models in two aspects: one of the two bending modes is inhibited because of the large width-to-thickness aspect-ratio, and the two remaining twisting and bending modes are governed by a *non-quadratic* strain energy potential that effectively captures the inextensible deformations of the ribbon mid-surface. Sadowsky's strain energy is non-convex, which can lead to the formation of a non-smooth solution representing a micro-structure [34,35]; to avoid these difficulties, we use the higher-order model of Wunderlich, which accounts for the dependence of the energy on the longitudinal gradient of bending and twisting strain [13].

The Wunderlich model has been solved numerically by a continuation method, see for instance the work of [15]. The continuation method is an extension of the shooting method, which can efficiently track solutions depending on a parameter [36]. It requires the full boundary-value problem of equilibrium to be specified, which is quite impractical in the case of Wunderlich ribbons. A recent and promising alternative is the high-order method of [22], which starts from linear and quadratic interpolations of the bending and twisting strains and treats the centerline position and the directors as secondary (reconstructed) quantities. In the present work, we explore an alternative approach, and show that simulations of the Wunderlich model are possible with limited additional work on top of the generic discrete elastic rod framework.

We build on the work of [16], which showns that the Wunderlich model can be viewed as a special type of a non-linear elastic rod, see also [37]. Accordingly, simulations of the Wunderlich

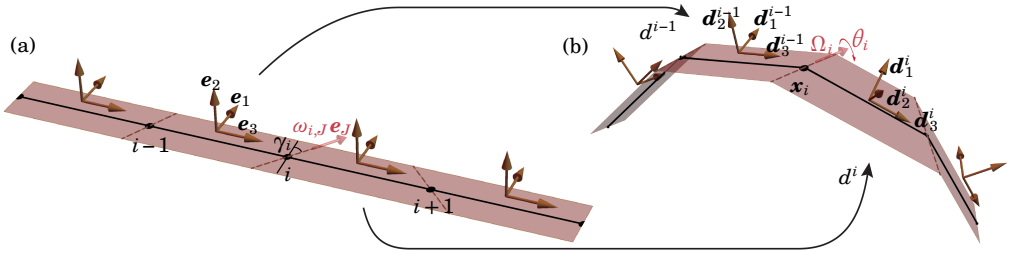

Figure 4.1. A discrete inextensible ribbon: (a) flat configuration and (b) current (folded) configuration obtained by folding along the generatrices (brown dashed lines) by an angle θ_i. By the inextensibility condition, the fold line through vertex $\boldsymbol{x}_i$ in the current configuration lies at the intersection of the adjacent faces, *i.e.*, of the planes spanned by $\boldsymbol{d}_1^{i-1}$ and $\boldsymbol{d}_3^{i-1}$ on the one hand and by $\boldsymbol{d}_1^i$ and $\boldsymbol{d}_3^i$ on the other hand.

model can be achieved using a simple extension of the Discrete elastic rod model, which we describe now. We first introduce a geometric model for a *discrete inextensible ribbon*, in which the inextensibility of the mid-surface is fully taken into account. We start from a rectangular strip lying in the plane spanned by $(\boldsymbol{e}_1, \boldsymbol{e}_3)$, as shown in Figure 4.1a. Through every node (shown as black dots in the figure), we pick a folding direction within the plane of the strip (brown dotted line in the figure); we denote by $\pi/2 - \gamma_i$ the angle of the fold line relative to the centerline. Next, we fold along each one of these lines by an angle θ_i, as shown in Figure 4.1b. We call the resulting surface a discrete inextensible ribbon. By construction, it is isometric to the original strip.

Let us now introduce the director frames $\boldsymbol{d}_I^i$ following rigidly each one of the faces: the planar faces are spanned by the directors $\boldsymbol{d}_1^i$ and $\boldsymbol{d}_3^i$. By construction the vector $\boldsymbol{\Omega}_i$ for the rotation that maps one frame, $\boldsymbol{d}_I^{i-1}$, to the next, $\boldsymbol{d}_I^i$, see equation (2.17), is aligned with the fold line. We observe that the unit tangent along the fold direction is $\boldsymbol{e}_3 \sin\gamma_i + \boldsymbol{e}_1 \cos\gamma_i$ in the flat configuration of the strip; it is therefore mapped to $\boldsymbol{d}_3^{i-1} \sin\gamma_i + \boldsymbol{d}_1^{i-1} \cos\gamma_i = \boldsymbol{d}_3^i \sin\gamma_i + \boldsymbol{d}_1^i \cos\gamma_i$ in the current configuration. In view of this, we conclude that

$$\boldsymbol{\Omega}_i = \left(\boldsymbol{d}_3^{i-1} \sin\gamma_i + \boldsymbol{d}_1^{i-1} \cos\gamma_i\right) \theta_i = \left(\boldsymbol{d}_3^i \sin\gamma_i + \boldsymbol{d}_1^i \cos\gamma_i\right) \theta_i.$$

Comparing with equation (2.18), we obtain the discrete deformation measure in the developable ribbon as $\omega_{i,1} = \theta_i \cos\gamma_i$ (bending mode), $\omega_{i,2} = 0$ (inhibited bending mode) and $\omega_{3,i} = 0$ (twisting mode). Eliminating θ_i, we find $\omega_{i,2} = 0$ and $\frac{\omega_{i,3}}{\omega_{i,1}} = \tan\gamma_i$, which can be rewritten in terms of the original discrete strain $\boldsymbol{\kappa}_i = (\kappa_{i,1}, \kappa_{i,2}, \kappa_{i,3})$ with the help of equation (2.15) as

$$\begin{aligned} \kappa_{i,2} &= 0 \\ \kappa_{i,3} &= \eta_i\, \kappa_{i,1}, \end{aligned} \tag{4.6}$$

where

$$\eta_i = \tan\gamma_i.$$

The continuous version of the developability conditions is $\kappa_2(s) = 0$ and $\kappa_3(s) = \eta(s)\,\kappa_1(s)$, where $\eta(s) = \tan\gamma(s)$ and $\pi/2 - \gamma(s)$ is the angle between the generatrix and the tangent, see for instance [16]. It is remarkable that the discrete developability conditions (4.6) are identically satisfied. This is a consequence of the simple geometric interpretation for the discrete deformation measures introduced in Section 2.

To simulate inextensible ribbons, we introduce the unknown η_i as an additional degree of freedom at each one of the interior nodes, and we use in equation (4.3) a strain energy density directly inspired by that of Wunderlich [15,16],

$$E_i(\boldsymbol{\kappa}_i, \eta_{i-1}, \eta_i, \eta_{i+1}) = \frac{D\,w}{2\,\ell} \kappa_{i,1}^2 \,(1+\eta_i^2)^2\, \frac{1}{w\,\eta_i'} \ln\left(\frac{1+\frac{1}{2}\,\eta_i'\,w}{1-\frac{1}{2}\,\eta_i'\,w}\right). \tag{4.7}$$

In equation (4.7), $D = \frac{Y\,h^3}{12\,(1-\nu^2)}$ is the bending modulus from plate theory, h is the thickness, w is the width and ℓ is the discretization length. The quantity η_i' is calculated by a central-difference approximation of the gradient of η,

$$\eta_i' = \frac{\eta_{i+1} - \eta_{i-1}}{2\,\ell},$$

where ℓ is the mesh size. The constraint $(4.6)_2$ is imposed at each node using the SQP method. Introducing the nodal degrees of freedom η_i together with the constraint $(4.6)_2$ allows us to work around calculating $\eta_i = \kappa_{i,3}/\kappa_{i,1}$, which is a division with a potentially small denominator; in addition, this approach warrants that $\kappa_{i,3} = 0$ whenever $\kappa_{i,1} = 0$, which is necessary for the Wunderlich energy to remain finite.

It is a feature of the Wunderlich model that η can take on arbitrary values in intervals where κ_1 vanishes identically. To work around this, we have introduced an artificial drag on the η_i's between iterations of the solve. When convergence is reached, the drag force is identically zero.

The discrete potential energy $\Phi(\boldsymbol{X})$ is minimized by the same numerical method as described in Section 4(a), taking into account the kinematic constraints (4.6) and the centerline inextensibility (4.4).

5. Illustrations

In this section, the Discrete elastic rod model is used to simulate

- a linearly elastic model for an isotropic beam, Section 5(a),
- a linearly elastic model for an anisotropic beam with natural curvature, Section 5(b),
- Sano and Wada's extensible ribbon model, Section 5(c),
- Wunderlich's inextensible ribbon model, Section 5(d).

These examples serve to illustrate the capabilities of the model. In addition, comparison with reference solutions available from the literature provides a verification of its predictions.

(a) Euler buckling

We consider Euler buckling for a planar, inextensible elastic rod that is clamped at one endpoint. We consider two types of loading: either a point-like force f_p at the endpoint opposite the clamp or a force f_d distributed along the length of the rod. In both cases, the force is applied along the initial axis of the rod, is invariable (dead loading) and is counted positive when compressive. A sketch is provided in Figure 5.1.

Mathematically, the equilibria of the rod having bending modulus B are the stationary points of the functional $\Phi = \int_0^L \frac{B}{2}\,\theta'^2(s)\,\mathrm{d}s + f_\mathrm{p}\,x(L)$ (point load) or $\Phi = \int_0^L \left(\frac{B}{2}\,\theta'^2(s) + f_\mathrm{d}\,x(s)\right)\,\mathrm{d}s$ (distributed load), subject to the clamping condition $\theta(0) = 0$. The coordinates of a point on the centerline $(x(s), y(s))$ are reconstructed using the inextensibility condition as $x(s)\,\boldsymbol{e}_1 + y(s)\,\boldsymbol{e}_2 = \int_0^s (\cos\theta\,\boldsymbol{e}_1 + \sin\theta\,\boldsymbol{e}_2)\,\mathrm{d}s$.

The boundary-value equilibrium problem for the Elastica is obtained by the Euler-Lagrange method as

$$0 = B\,\theta''(s) + \sin\theta(s) \times \begin{cases} f_\mathrm{p} & \text{(point-like load)} \\ f_\mathrm{d}\,(L-s) & \text{(distributed load)} \end{cases} \qquad \theta(0) = 0 \qquad \theta'(L) = 0. \tag{5.1}$$

By writing this problem in dimensionless form, one can effectively set the bending modulus, the length and the load to $B = 1$, $L = 1$, and $f_\mathrm{p} = \overline{f}_\mathrm{p}$ (point-like load) or $f_\mathrm{d} = \overline{f}_\mathrm{d}$ (distributed load),

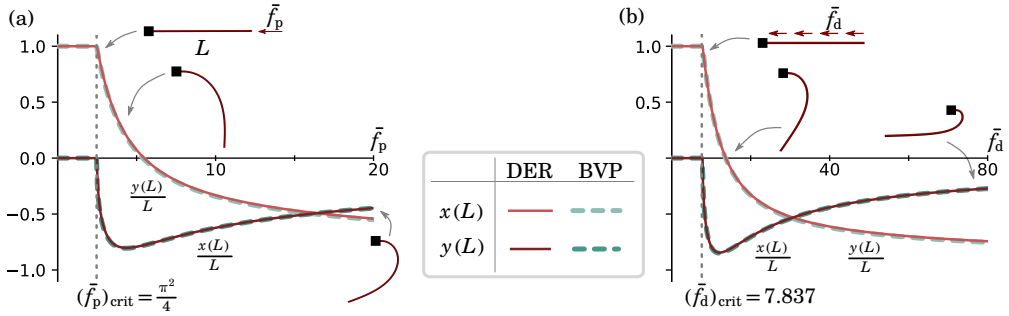

Figure 5.1. Buckling of a planar Elastica subject to (a) a point-like force applied at the endpoint and (b) a distributed force. Comparison of the solutions of the boundary-value problem (5.1) by a numerical shooting method (dashed curves) and of the Discrete elastic rod method (solid curves): the scaled coordinates of the endpoint $s = L$ are plotted as a function of the dimensionless load. The dotted vertical line is the first critical load predicted by a linear bifurcation analysis from equation (5.3).

where the dimensionless load is

$$\overline{f}_{\mathrm{p}} = \frac{f_{\mathrm{p}}}{B/L^2}, \qquad \overline{f}_{\mathrm{d}} = \frac{L\, f_{\mathrm{d}}}{B/L^2}. \tag{5.2}$$

The critical buckling loads are found by solving the *linearized* version of the buckling problem (5.1) (linear bifurcation analysis),

$$\begin{aligned} \left(\overline{f}_{\mathrm{p}}\right)_{\mathrm{crit}} &= \frac{\pi^2}{4} \qquad \text{(point-like load)} \\ \left(\overline{f}_{\mathrm{d}}\right)_{\mathrm{crit}} &= 7.837 \qquad \text{(distributed load)} \end{aligned} \tag{5.3}$$

Numerical simulations of this Euler buckling problem are conducted using the discrete elastic rod method, as explained in Section 4.3. Simulations are set up with $B = 1$, $L = 1$ and number of nodes $N = 100$. In view of this we expect the buckling loads to be $f_{\mathrm{d}} = \overline{f}_{\mathrm{d}}$ $f_{\mathrm{p}} = \overline{f}_{\mathrm{p}}$. The inextensibility constraint is enforced exactly using the SQP method. The clamped boundary is enforced by fixing the first and second nodes as well as the first frame.

The typical simulation time is about 0.1 s for each equilibrium on a personal computer; the results are shown in Figure 5.1 and are compared to those obtained by solving (5.1) using the `bvp4c` solver from Matlab. A good agreement on the position of the endpoint of the rod is found in the entire post-bifurcation regime. In addition, the onset of bifurcation agrees accurately with the prediction (5.3) from the linear stability analysis.

(b) Folding of an over-curved ring

A circular elastic ring with length L can buckle out of plane if its natural natural curvature $\kappa_{(0)}$ does not match the curvature $2\pi/L$ of the circle with length L. In the case of an over-curved ring, such that $\kappa_{(0)} > 2\,\pi/L$, a buckled shape featuring two symmetric lobes has been reported [33,38, 39]. Here, we simulate the buckling of over-curved rings using the discrete elastic rod model and compare the results with the experimental shapes reported by [38].

In the experiments of [38], a commercial Slinky spring with a width $w = 5$ mm, thickness $t = 2$ mm and length $L = 314$ mm is used; Poisson's ratio has been measured as $\nu = 0.41$. Note that the aspect-ratio $t/w = 0.4$ is not small. In our simulations, we use a discrete version of the quadratic strain energy for a linearly elastic rod having an anisotropic cross-section ($I_1 \neq I_2$), see equations (4.1–4.3). We use the elastic moduli reported in the supplement of [38],

$$Y\, I_1 = Y\, \frac{w\, t^3}{12}, \qquad Y\, I_2 = Y\, \frac{w^3\, t}{12}, \qquad \mu\, J = Y\, \frac{0.256\, w\, t^3}{2\,(1+\nu)}. \tag{5.4}$$

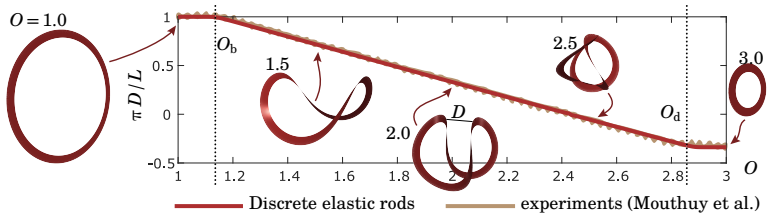

Figure 5.2. Equilibrium of an over-curved elastic ring. Material and geometric parameters correspond to the Slinky used by [38] (see main text for values). a) Equilibrium configurations for different values of the over-curvature ratio O. b) Minimal distance of approach D as a function of O: comparison of Discrete elastic rod simulations and experiments [38]. The simulations reproduce both the initial buckling at O_b and the 'de-buckling' into a flat, triply covered ring at O_d.

The value 0.256 in the numerator was obtained by [38] from the book of [40], and applies to the particular commercial Slinky used in their experiments. In the absence of applied loading, the value of the Young modulus is irrelevant and we set $Y = 1$ in the simulations.

The equilibria of the Discrete elastic rod are calculated numerically for different values of the dimensionless loading parameter $O = 2\,\pi\,\kappa_{(0)}/L$, with $O > 1$ corresponding to the over-curved case. We use $N = 400$ nodes. We start from a circular configuration having curvature $\kappa_{(0)} = 2\,\pi/L$. The Discrete elastic rod model is closed into a ring as follows: the first two nodes and the last two nodes are prescribed to $\boldsymbol{x}_0 = \boldsymbol{x}_{N-1} = \boldsymbol{0}$ and $\boldsymbol{x}_1 = \boldsymbol{x}_N = \ell\,\boldsymbol{e}_x$, respectively; the first and last frames are also fixed, such that $\boldsymbol{d}_1^0 = \boldsymbol{d}_1^{N-1} = \boldsymbol{e}_y$. Next, the over-curvature $\kappa_{(0)}$ is varied incrementally. For each value of $\kappa_{(0)}$, an equilibrium configuration is sought, and we extract the minimal distance D between pairs of opposite points on the ring. In Figure 5.2, the scaled distance D is plotted as a function of O. A good agreement is found with the experiments over the entire range of values of the over-curvature parameter $O > 1$. The simulations correctly predict a planar, triply covered circular solution for $O > O_\mathrm{d} \approx 2.85$, as seen in the experiments.

(c) Buckling of a bent and twisted ribbon

We now turn to an effective rod model applicable to thin ribbons. Sano and Wada [41] have proposed an effective beam model that accounts for the stretchability of the ribbon having moderate width, thereby improving on Sadowsky's inextensibility assumption. A discrete version of their continuous model is of the form (4.3) with a strain energy per elastic hinge

$$E_i(\kappa_1, \kappa_2, \kappa_3) = \frac{1}{2\,\ell}\left(A_1\,\kappa_1^2 + A_2\left(\kappa_2^2 + \frac{\kappa_3^4}{\ell^2/\xi^2 + \kappa_2^2}\right) + A_3\,\kappa_3^2\right). \tag{5.5}$$

Here, ℓ is the uniform segment length in the undeformed configuration, $A_1 = Y\,h\,w^3/12$ and $A_2 = Y\,h^3\,w/12$ are the initial bending moduli, $A_3 = Y\,h^3\,w/[6\,(1+\nu)]$ is the initial twisting modulus and $\xi^2 = (1-\nu^2)\,w^4/60\,h^2$. The parameter ξ is the typical length-scale, where the stretchability of the mid-surface starts to play a role. The potential E_i from equation (5.5) is non-quadratic, meaning that the equivalent rod has non-linear elastic constitutive laws.

The elastic model (5.5) of Sano and Wada is applicable to thin ribbons, such that $w \gg h$. It is based on kinematic approximations. A refined version of their model has been obtained very recently by [17], by asymptotic expansion starting from shell theory; in the latter work, a detailed discussion of the validity of the various models for thin ribbons can also be found. We do not expect any difficulty in applying the present numerical model to the ribbon model in [17]. Both the models of Sano and Wada and of Audoly and Neukirch improve on the Wunderlich model by addressing the stretchability of the ribbon; unlike the Wunderlich model, however, they ignore the dependence of the energy on η', and therefore account less accurately for the 'conical' singularities often observed in ribbons [42] as η varies quickly there.

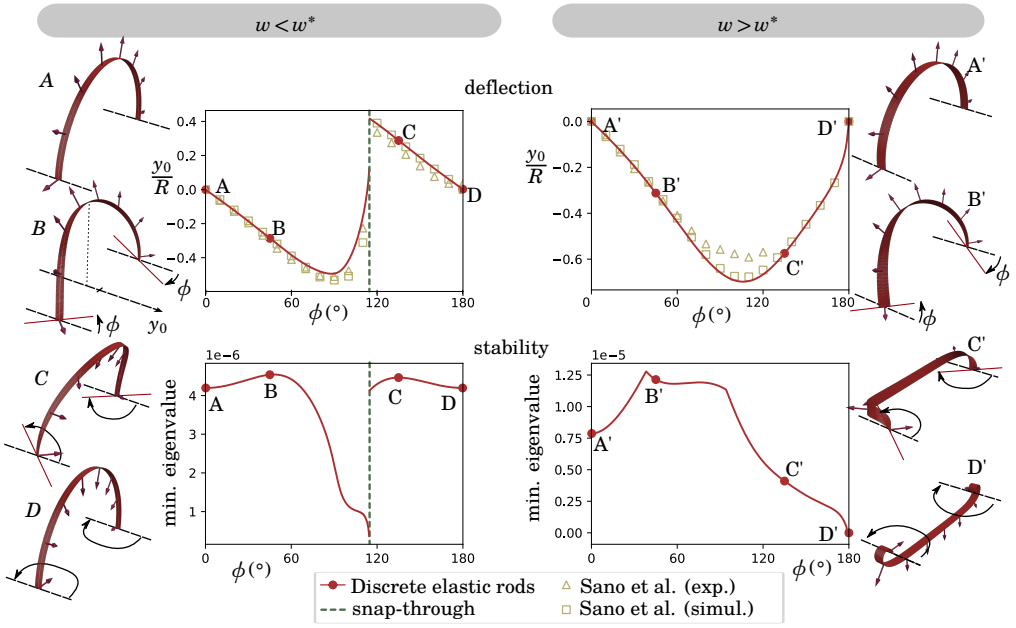

Figure 5.3. Equilibria of an extensible ribbon, as captured by Sano and Wada's equivalent rod model, see equation (5.5). *Top row*: equilibrium diagram showing the scaled value of the deflection y_0 at the center of the ribbon as a function of the twisting angle ϕ at the endpoints. Comparison of the experiments (triangles) and simulations (squares) from [41] with simulations using the Discrete elastic rod model (solid curves and circles). *Left column*: moderately wide ribbon $(h, w, R) = (0.2, 8, 108)$mm showing a snapping instability; *Right column*: wider ribbon $(h, w, R) = (0.2, 15, 108)$mm, in which the instability is suppressed. *Bottom row*: smallest eigenvalues of the tangent stiffness matrix, on the same solution branch as shown in the plot immediately above: the presence of an instability for $w < w^*$ (left column) is confirmed by the fact that the smallest eigenvalue reaches zero when the instability sets in.

Following [41], we consider the buckling of a ribbon with length $L = \pi R$ bent into half a circle, whose ends are twisted in the opposite sense by an angle ϕ, see Figure 5.3. Specifically, they identified a snapping instability which occurs for moderately wide ribbons, when the width $w < w^*$ is below a threshold $w^* \approx 1.24\sqrt{L\,h}$, but not for wider ribbons, when $w > w^*$; they showed that their equivalent rod model can reproduce this instability, as well as its disappearance for larger widths. In Figure 5.3, we compare the predictions of a discrete elastic rod model using (5.5) with the original experiments and simulations from [41]. Our simulations use $N = 350$ vertices each. Our simulation results are in close agreement with both their experimental and numerical results. In particular, we recover the instability when $w < w^*$ only.

(d) The elastic Möbius band

An extension of the Discrete elastic rod model that simulates the inextensible ribbon model of Wunderlich has been described in Section 4(b), see equation (4.7). With the aim of illustrating and verifying this discrete model, we simulate the equilibrium of a Möbius ribbon, and compare the results with those reported in the seminal paper of Starostin and van der Heijden [14]. In our simulations, the inextensible strip is first bent into a circle, and the endpoints are twisted progressively by an angle of 180° to provide the correct topology. The final equilibrium shapes are then recorded for all possible values of the aspect-ratio w/L. For these final equilibrium shapes, the conditions $\boldsymbol{x}_0 = \boldsymbol{x}_{N-1} = \boldsymbol{0}$ and $\boldsymbol{x}_1 = \boldsymbol{x}_N = \ell\,\boldsymbol{e}_x$ hold as earlier, and the orientation of the terminal material frames are such that $\boldsymbol{d}_1^0 = +\boldsymbol{e}_y$ and $\boldsymbol{d}_1^{N-1} = -\boldsymbol{e}_y$.

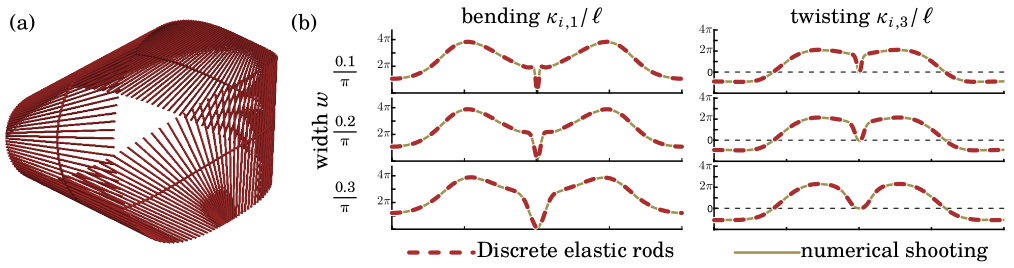

Figure 5.4. Simulation of an inextensible Möbius strip with $L = 1$. (a) Equilibrium width $w = 1/(2\pi)$, as simulated by the Discrete elastic rod model from Section 4(b) with $N = 150$ nodes. (b) Distribution of bending and twisting: Discrete elastic rod simulations with $N = 250$ vertices (dashed curves) versus the solution of [14] obtained by numerical shooting (solid curves); the latter have been properly rescaled to reflect our conventions.

The equilibrium shape for a particular aspect-ratio $w/L = 1/(2\pi)$ is shown in Figure 5.4a, with arc-length $L = 1$, width $w = 1/(2\pi)$ and $N = 150$ simulation nodes. A detailed comparison with the results of [14] is provided in Figure 5.4b, where the scaled bending and twisting strains $\kappa_{i,1}/\ell$ and $\kappa_{i,3}/\ell$ from the discrete model with $N = 250$ vertices are compared with the strains $\kappa_1(s)$ and $\kappa_3(s)$ obtained by [14] using numerical shooting, for different values of the width w.

6. Conclusion

We have presented a new formulation of the Discrete elastic rod model. The formulation is concise and uses only the minimally necessary degrees of freedom: the position of the nodes and the angle of twist of the segments between the nodes. It naturally incorporates the adaptation condition without the need for any constraint, penalty or Lagrange multiplier. We use bending and twisting deformation measures that are different from those used in earlier work on discrete elastic rods, are equally consistent with their continuum counterparts and have a simple physical interpretation in the discrete setting. Consequently, the formulation is versatile in the sense that it can be combined with a variety of linear and nonlinear as well as elastic and inelastic constitutive relations. In fact, ribbons can be incorporated as generalized rods with a nonlinear constitutive model. We have focused on static problems in this paper; the extension to dynamic simulations can be done along the same lines as in earlier work on discrete elastic rods.

We have presented explicit formulae for the first and second derivatives of the deformation measures that ease implementation. We have demonstrated our method with four examples, and verified our results against prior experimental and theoretical findings in the literature.

Data Accessibility. The source code used for the numerical simulation is available through CaltechDATA at https://data.caltech.edu/badge/latestdoi/425059053.

Authors' Contributions. All three authors conceived of the work and the formulation. KK conducted the theoretical and numerical calculations with advice from BA and KB. KK and BA took the lead in writing the manuscript and all three authors finalized it.

Competing Interests. The authors declare that there are no competing interests.

Funding. The work began when BA visited Caltech as a Moore Distinguished Scholar. KK and KB gratefully acknowledge the support of the US Office of Naval Research through Multi-investigator University Research Initiative Grant ONR N00014-18-1-2624.

References

1. Baek C, Reis PM. 2019 Rigidity of hemispherical elastic gridshells under point load indentation. *Journal of the Mechanics and Physics of Solids* **124**, 411–426.

2. Panetta J, Konaković-Luković M, Isvoranu F, Bouleau E, Pauly M. 2019 X-Shells: A New Class of Deployable Beam Structures. *ACM Transactions on Graphics (TOG)* **38**, 1–15.
3. Antman S. 2005 *Nonlinear problems of elasticity*. Springer-Verlag.
4. Audoly B, Pomeau Y. 2010 *Elasticity and geometry: from hair curls to the nonlinear response of shells*. Oxford University Press.
5. Brun PT, Ribe NM, Audoly B. 2012 A numerical investigation of the fluid mechanical sewing machine. *Physics of fluids* **24**, 043102.
6. Ribe NM, Habibi M, Bonn D. 2012 Liquid rope coiling. *Annual Review of Fluid Mechanics* **44**, 249–266.
7. Coleman BD, Newman DC. 1988 On the rheology of cold drawing. I. Elastic materials. *Journal of Polymer Science: Part B: Polymer Physics* **26**, 1801–1822.
8. Audoly B, Hutchinson JW. 2016 Analysis of necking based on a one-dimensional model. *Journal of the Mechanics and Physics of Solids* **97**, 68–91.
9. Audoly B, Hutchinson JW. 2019 One-dimensional modeling of necking in rate-dependent materials. *Journal of the Mechanics and Physics of Solids* **123**, 149–171.
10. Lestringant C, Audoly B, Kochmann DM. 2020 A discrete, geometrically exact method for simulating nonlinear, elastic or non-elastic beams. *Computer Methods in Applied Mechanics and Engineering* **361**, 112741.
11. Lestringant C, Audoly B. 2020 A one-dimensional model for elasto-capillary necking. *Proceedings of the Royal Society A* **476**.
12. Sadowsky M. 1929 Die Differentialgleichungen des Möbiusschen Bandes. In *Jahresbericht der Deutschen Mathematiker-Vereinigung* vol. 39 (2. Abt. Heft 5/8) pp. 49–51.
13. Wunderlich W. 1962 Über ein abwickelbares Möbiusband. *Monatshefte für Mathematik* **66**, 276–289.
14. Starostin EL, van der Heijden GHM. 2007 The shape of a Möbius strip. *Nature Materials* **6**, 563–567.
15. Starostin EL, van der Heijden GHM. 2015 Equilibrium Shapes with Stress Localisation for Inextensible Elastic Möbius and Other Strips. *Journal of Elasticity* **119**, 67–112.
16. Dias MA, Audoly B. 2015 "Wunderlich, meet Kirchhoff": A general and unified description of elastic ribbons and thin rods. *Journal of Elasticity* **119**, 49–66.
17. Audoly B, Neukirch S. 2021 A one-dimensional model for elastic ribbons: a little stretching makes a big difference. *Journal of the Mechanics and Physics of Solids* **153**, 104457.
18. Bergou M, Wardetzky M, Robinson S, Audoly B, Grinspun E. 2008 Discrete Elastic Rods. *ACM Transactions on Graphics* **27**, 63:1–63:12.
19. Steigmann DJ, Faulkner MG. 1993 Variational theory for spatial rods. *Journal of Elasticity* **33**, 1–26.
20. Bertails F, Audoly B, Cani MP, Querleux B, Leroy F, Lévêque JL. 2006 Super-Helices for Predicting the Dynamics of Natural Hair. In *ACM Transactions on Graphics* pp. 1180–1187.
21. Casati R, Bertails-Descoubes F. 2013 Super Space Clothoids. *ACM Transactions on Graphics* **32**.
22. Charrondière R, Bertails-Descoubes F, Neukirch S, Romero R. 2020 Numerical modeling of inextensible elastic ribbons with curvature-based elements. *Computer Methods in Applied Mechanics and Engineering* **364**, 112922.
23. Jawed MK, Novelia A, O'Reilly OM. 2017 *A primer on the kinematics of discrete elastic rods*. Springer.
24. Gazzola M, Dudte LH, McCormick AG, Mahadevan L. 2018 Forward and inverse problems in the mechanics of soft filaments. *Royal Society Open Science* **5**.
25. Morais JP, Georgiev S, Sprößig W. 2014 An Introduction to Quaternions. *Real Quaternionic Calculus Handbook*.
26. Linn J. 2020 Discrete Cosserat Rod Kinematics Constructed on the Basis of the Difference Geometry of Framed Curves—Part I: Discrete Cosserat Curves on a Staggered Grid. *Journal of Elasticity* pp. 177–236.
27. Bergou M, Audoly B, Vouga E, Wardetzky M, Grinspun E. 2010 Discrete Viscous Threads. *Transactions on Graphics* **29**, 116.
28. Audoly B, Clauvelin N, Brun PT, Bergou M, Grinspun E, Wardetzky M. 2013 A discrete geometric approach for simulating the dynamics of thin viscous threads. *Journal of Computational Physics* **253**, 18–49.
29. Nocedal J, Wright SJ. 2006 *Numerical Optimization*. Springer New York.
30. Guennebaud G, Jacob B et al.. 2010 Eigen v3. http://eigen.tuxfamily.org.

31. Yu Y, Nakano M, Ikeda T. 2003 Photomechanics: Directed bending of a polymer film by light. *Nature* **425**, 145–145.
32. Gelebart AH, Mulder DJ, Varga M, Konya A, Vantome G, Meijer EW, Selinger RLB, Broer DJ. 2017 Making waves in a photoactive polymer film. *Nature* **546**, 632–636.
33. Bae J, Na JH, Santangelo CD, Hayward RC. 2014 Edge-defined metric buckling of temperature-responsive hydrogel ribbons and rings. *Polymer* **55**, 5908–5914.
34. Freddi L, Hornung P, Mora MG, Paroni R. 2015 A corrected Sadowsky functional for inextensible elastic ribbons. *Journal of Elasticity* **123**, 125–136.
35. Paroni R, Tomassetti G. 2019 Macroscopic and Microscopic Behavior of Narrow Elastic Ribbons. *Journal of Elasticity* pp. 409–433.
36. Doedel EJ, Champneys AR, Fairgrieve TF, Kuznetsov YA, Sandstede B, Wang XJ. 2007 AUTO-07p: continuation and bifurcation software for ordinary differential equations. See http://indy.cs.concordia.ca/auto/.
37. Starostin EL, van der Heijden GHM. 2009 Force and moment balance equations for geometric variational problems on curves. *Physical Review E* **79**, 066602.
38. Mouthuy PO, Coulombier M, Pardoen T, Raskin JP, Jonas AM. 2012 Overcurvature describes the buckling and folding of rings from curved origami to foldable tents. *Nature Communications* **3**, 1–8.
39. Audoly B, Seffen KA. 2015 Buckling of naturally curved elastic strips: the ribbon model makes a difference. *Journal of Elasticity* **119**, 293–320.
40. Ugural AC, Fenster SK. 2019 *Advanced mechanics of materials and applied elasticity*. International Series in the Physical and Chemical Engineering Sciences. Prentice Hall.
41. Sano TG, Wada H. 2019 Twist-Induced Snapping in a Bent Elastic Rod and Ribbon. *Physical Review Letters* **122**, 114301.
42. Yu T, Hanna JA. 2019 Bifurcations of buckled, clamped anisotropic rods and thin bands under lateral end translations. *Journal of the Mechanics and Physics of Solids* **122**, 657–685.